Full-wave simulation of the forward scattering of sound in a structured ocean: A comparison with observations

Michael A. Wolfson[a]
Earth System Science Center, Pennsylvania State University, University Park, Pennsylvania 16802

John L. Spiesberger[b]
Department of Meteorology, Pennsylvania State University, University Park, Pennsylvania 16802

Between 1983 and 1989, acoustic pulse-like signals at 133-Hz, 60-ms resolution, were transmitted from Oahu to Northern California. Analysis of the data indicates that the early arriving, steep paths are stable over basin scales, whereas the late, near-axial paths are sensitive to ocean structure. The late paths undergo vertical scattering on the order of the acoustic waveguide, i.e., 1 km [J. Acoust. Soc. Am. **99**, 173–184 (1996)]. The parabolic approximation is used to simulate pulse propagation over the vertical plane connecting the source and receiver. Several prescriptions are used for the speed of sound: (1) Climatologically averaged sound speed with and without a realization of internal waves superposed; (2) Measured mesoscale structure with and without a realization of internal waves superposed. The spectrum of the internal waves is given by Garrett and Munk. Modeled internal waves and the measured mesoscale structure are sufficient to explain the vertical scattering of sound by 1 km. The mesoscale structure contributes a travel time bias of 0.6 s for the late multipath. This bias is seen to be a relevant contribution in accounting for the travel times of the last arrival. © *1999 Acoustical Society of America.* [S0001-4966(99)03108-2]

PACS numbers: 43.30.Dr, 43.30.Rc [DLB]

INTRODUCTION

In a recent paper by Spiesberger and Tappert,[1] geometric acoustics was utilized to interpret long range receptions of acoustic signals transmitted from the Kaneohe source.[2] The experiment involved propagation of 133-Hz, 60-ms resolution pseudo-random signals over a distance of 3709.21 km. Geometric acoustics applied to an environment that included mesoscale structure was able to adequately model the early arriving, resolved stable acoustic multipaths, which were derived by incoherently averaging over the receptions that occurred each day. However, the coda of about one second could not be accounted for with ray or full-wave theory. They hypothesized that forward scattering due to internal gravity waves in addition to mesoscale structure is responsible for vertically scattering the acoustic energy a distance of 1 km from the axis of the sound channel. Recent studies by Colosi and Flatté[3] and Colosi[4] of wave propagation through internal wave fields provide additional credence to this hypothesis, but our studies reveal that the effect of ocean mesoscale structure is important as well. To test the hypothesis, we resort to full-wave modeling, using a parabolic approximation to the one-way Helmholtz wave equation (PE). Numerical simulations based on this model support the hypothesis that acoustic energy interacting with internal waves, mesoscale structure, and the bottom are responsible for vertically scattering the late arriving axial energy by 1 km.

Note that PE simulations at multi-megameter ranges, through ocean environments which include internal waves, have been performed and recently reported in the literature by Colosi and Flatté,[3] and Colosi.[4] Our efforts using these type of simulations differ in that we compare the results to particular observations, more in line with what has been done by Colosi *et al.* at the shorter range of one megameter.[5]

We proceed by the following prescription. Section I describes the Kaneohe experiment. In Sec. II the method used to generate the sound speed fields is described. Much of this section involves describing the method used to model the range dependent sound speed perturbations due to internal waves, although it is not terribly different from what Colosi *et al.*[5] have done. Section III describes the parabolic equation model. Near the source and receiver, sub-bottom interaction is significant, controlling convergence characteristics of the parabolic equation model over other environmental constituents, such as internal waves. To optimize code performance while still satisfying convergence, a variable depth and range step size is used. In Sec. IV the model results are presented and compared with observed impulse response data. Comparisons are made using four different ocean environments: climatological average and measured mesoscale structure, each with and without a realization of an internal wave field superposed. The primary objective being established, Sec. V describes a method for measuring the extent of vertical scattering as a function of range. Finally, Sec. VI discusses the relevance of our findings in regard to tomographic measurements.

Before proceeding to the main development of the paper, let us briefly outline the problem setting. The ocean to first order acts as a waveguide in depth for acoustic pulse transmissions in deep ocean mid-latitude environments. In-homogeneities in the sound speed field due to oceanic pro-

---

[a]Present address: Department of Physics, Washington State University, Pullman, WA 99164-2814.
[b]Also at: The Applied Research Laboratory, Pennsylvania State University, University Park, PA 16802. Present address: Department of Earth and Environmental Science, University of Pennsylvania, Philadelphia, PA 19104.
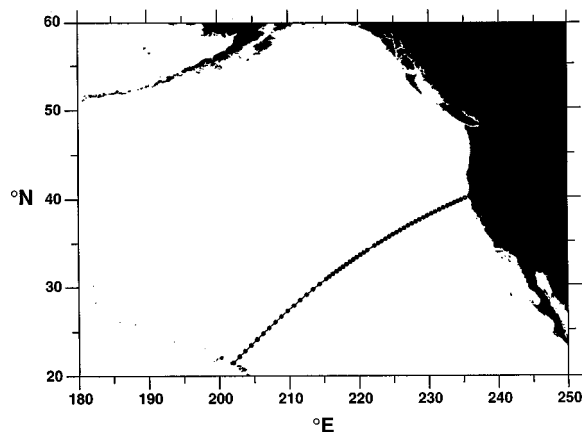
FIG. 1. Plan view of the Kaneohe source experiment. The source is located about five miles north of Kaneohe Bay, Oahu. The receiver near the coast of Northern California, is one of many U.S. Navy SOSUS stations used to receive these transmissions. Circles indicate the positions of 56 stations where conductivity, temperature, and depth were measured with a CTD in July 1988 by the Naval Oceanographic Office. Adapted from Ref. 1.

cesses such as mesoscale energetics and internal waves have scales that are large compared to the acoustic wavelength. They are weak in the sense that the deviation in the rms scattering angle due to interaction with a ''scatterer'' relative to that which would have taken place without the scatterer present is small compared to unity. It is in this sense that we refer to the problem as one of *multiple forward scattering*.

I. KANEOHE EXPERIMENT

The Kaneohe experiment consists of an acoustic source, bottom-mounted off the coast of Kaneohe Bay, Oahu, and a set of U.S. Navy Sound Surveillance Systems (SOSUS) spread out in the eastern North Pacific. The source, located at 21.512 35 °N, 202.228 48 °E, at a depth of 183 m (one meter above the ocean floor), transmitted acoustic pulse-like signals at 133-Hz, 60-ms resolution intermittently over the years 1983 to 1989. The receiver of interest in this study is located off the coast of Northern California (on the ocean floor), at 40.0786 °N, 234.8880 °E at a depth of 1433 m. Geographical locations are given in WGS-84.[6] Conductivity, temperature, and depth were recorded using a CTD to depths of about 2000 m at 56 stations along the geodesic (Fig. 1). Actual CTD depths are shown in Fig. 2. Travel times were measured using clock accuracies of 1 ms. The bathymetry along the geodesic is illustrated in Fig. 3. Further details of the experiment are found elsewhere.[1,2]

Interannual changes in travel time were measured to be about ±0.2 s. Rossby waves linked to ENSO are the dominant mechanism affecting the observed changes in travel time throughout the six-year experiment.[7] Most of the results of the analyses here do not depend on this change in travel time because the primary interpretation is based on the difference in travel time between the stable multipath and the late arriving energy.

To mitigate the stochastic effects on the received signal due to internal waves and increase the signal-to-noise ratio, daily incoherent averaging was performed. Anywhere from 70 to about 700 pulse-like signals per day were used to per-

form the average, and the representative data we chose are modeled results (see Fig. 4) using about 700 pulse-like signals transmitted and received on 29 November, 1983. Further details regarding the processing of the data can be found in Ref. 1.

II. MODELS OF OCEAN SOUND SPEED

Four distinct sound speed fields are used for the simulations presented in this paper, and they are designated as: (a) climatology; (b) mesoscale; (c) internal waves; (d) mesoscale and internal waves.

The climatology sound speed field is derived from a historical database of salinity and temperature, and is representative of the average profile which is horizontally smooth. The primary variation seen in this sound speed field is a shoaling of the sound channel axis from the source to receiver (Fig. 4 of Ref. 2). The mesoscale sound speed field contains deterministic mesoscale structure derived from 56 CTDs taken along the source–receiver geodesic in July 1988. We use the word mesoscale to denote sound speed inhomogeneities whose horizontal scales range from 25 km to 500 km, and which evolve on time scales of one month. The sound speed field denoted as ''internal waves'' represents sound speed fluctuations from internal waves superposed onto the climatology sound speed field. The ''mesoscale and internal waves'' sound speed field represents the mesoscale sound speed field with fluctuations due to internal waves superposed.

To describe the ocean sound speed fields, we first define a local Cartesian coordinate system for the vertical plane connecting the source and receiver along the geodesic. Let x measure the horizontal range in kilometers from the source, and z measure the depth in meters positive downward from the ocean surface. The ocean surface is taken to be flat. The sound speed fields (a) through (d) are computed on a discrete grid (x_i, z_j), $i = 1,...,i_{max}$, $j = 1,...,j_{max}$, which is determined by the smallest internal wave scales.

A. Climatology

To compute the climatological sound speed field, salinity and temperature data are extracted from the Levitus database.[8] Bilinear interpolation is then used to compute the temperature and salinity profiles at the range points x_i, $i = 1,...,i_{max}$, at the standard Levitus depths. The range points x_i are determined by $x_i = (i-1)\Delta x$, with Δx chosen to be about 312.5 m. This sets the shortest horizontal internal wave scale to be about 625 m. Del Grosso's formula[9] is then used to compute the sound speed at Levitus' standard depths. Finally, a quadratic spline is used to interpolate sound speeds onto discrete depths z_j. The discrete depths used are every 5 m from the surface down to 500 m, every 20 m from 500 m down to 3020 m, and every 50 m from 3020 m to the bottom of the water column. This interpolation algorithm avoids discontinuities in the sound speed gradient at Levitus' standard depths.[10]

B. Mesoscale

The mesoscale structure is interpolated onto the same (x_i, z_j) grid in a similar manner (Fig. 2). The CTD data are
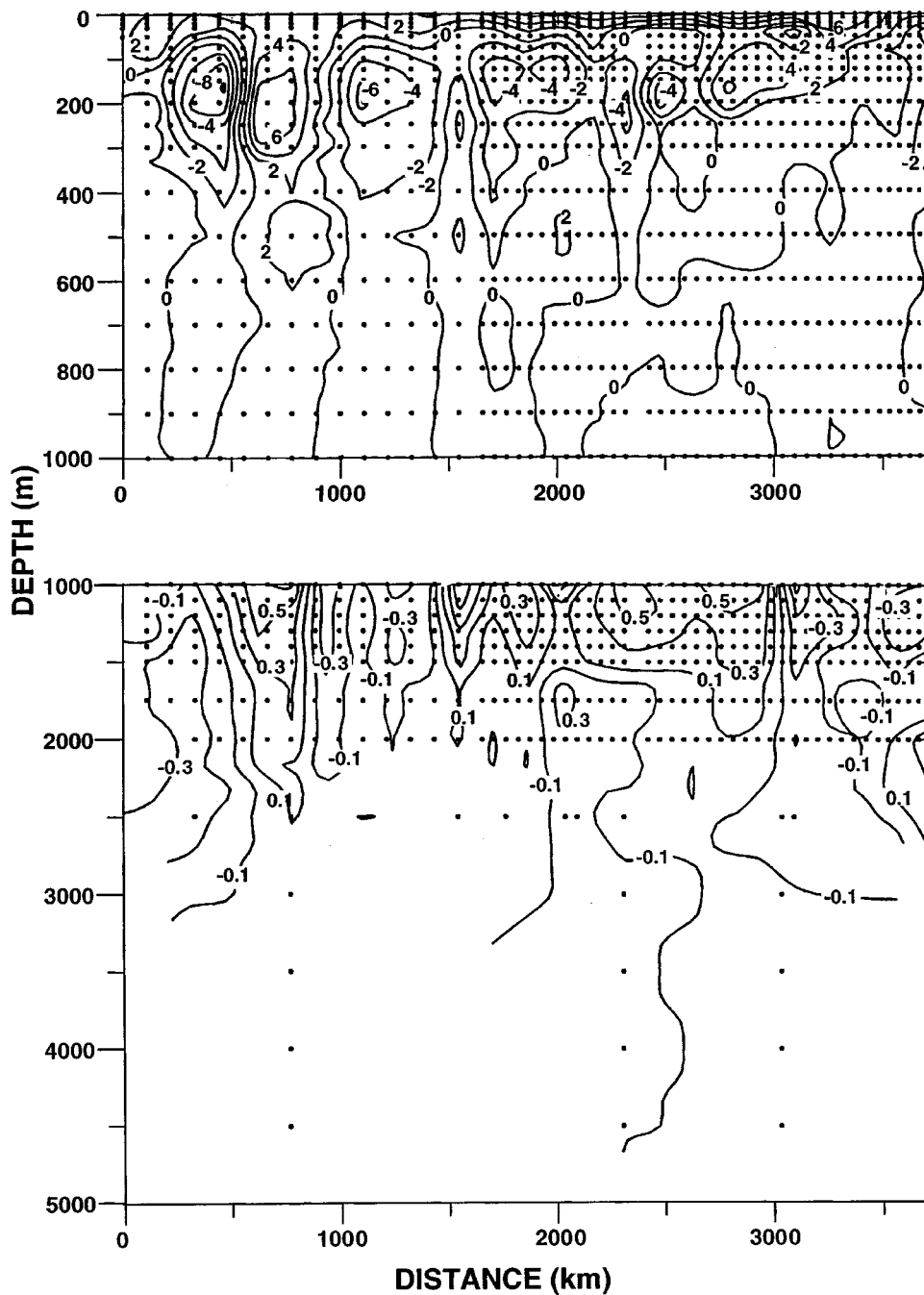
FIG. 2. Sound speeds computed from the July 1988 CTD cruise minus sound speeds computed from Levitus' climatology for the months May, June, and July. Negative values indicate the CTD section is colder and slower than Levitus' data. Contour intervals are 2 m/s and 0.2 m/s in the upper and lower panels, respectively. The dots indicate where the data were taken from the CTD. Adapted from Ref. 1.

linearly interpolated in range onto the points x_i. The same quadratic spline algorithm is then used to interpolate onto the depths z_j. From the source out to 1700 km, the horizontal resolution is about 225 km, and beyond this range to the receiver the horizontal resolution is about 112 km.

C. Internal waves

As mentioned above, the "internal waves" and "mesoscale and internal waves" sound speed fields involve superposing the sound speed fluctuations due to internal waves onto either the climatology or mesoscale sound speed field. Thus it is only necessary to describe how the sound speed fluctuations due to internal waves are modeled.

The method used to model internal waves is similar to what Colosi et al.[5] have done. Differences will be pointed

out as the description is elucidated. The basic premise is to partition the gridded vertical plane (x_i, z_j) into M overlapping horizontal "sections." The size of each section is about 80 km, and the extent of overlap is 10 km. Within each section, the ocean is nearly horizontally stratified, so that the buoyancy frequency $N(z_j)$, inertial frequency ω_i, and bottom depth z_{bot} are all range independent. Bathymetry was measured to an accuracy of within 2% of the total depth from the source out to about 130 km, and measured to within 50 m over the last 100 km along the geodesic. Bathymetry was extracted at 9-km intervals from ETOPO5[11] between these two regions. The actual bottom depth used for each section is range averaged from the measured and extracted bathymetry.

Internal waves which are based on the empirical spectrum of Garrett and Munk[12,13] are computed for each section.
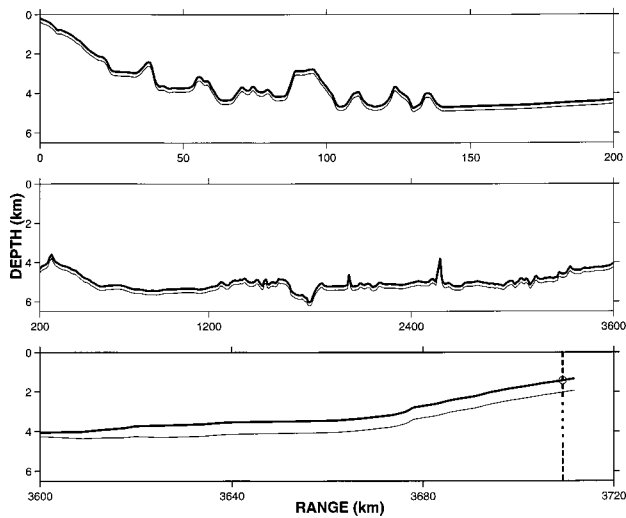
FIG. 3. Bathymetry (thick solid) and sediment-basement interface (thin solid) along Kaneohe geodesic for three different simulation domains: (1) near source bottom-limited, (2) deep ocean waveguide, (3) near receiver bottom-limited. The bathymetry was filtered using a 1-km horizontal length scale, and was extracted from the ETOPO5 database (Ref. 11).

Fully three-dimensional internal wave fields in a local Cartesian coordinate system are constructed, but only the wave field along the section is saved. The sections are then overlapped and smoothly patched together to form the total field of internal waves. The choice of using a three-dimensional internal wave field representation instead of a two-dimensional representation came from our inability to justify an approximation used by Dozier and Tappert.[14] The approximation involves the internal wave eigenfunctions that depend on the magnitude of horizontal wave number. They approximate these eigenfunctions by the eigenfunctions that depend on the component of horizontal wave number parallel to the section. When both components of the horizontal wave number are of the same order, and they are each small enough that the spectral weighting is significant, this approximation breaks down.

The method used to generate each section of internal waves, and the method by which sections are patched together is described in Appendix A. If $\delta c(x_i, z_j)$ denotes the vertical plane of gridded sound speed fluctuations due to internal waves, the total sound speed fields are expressed as
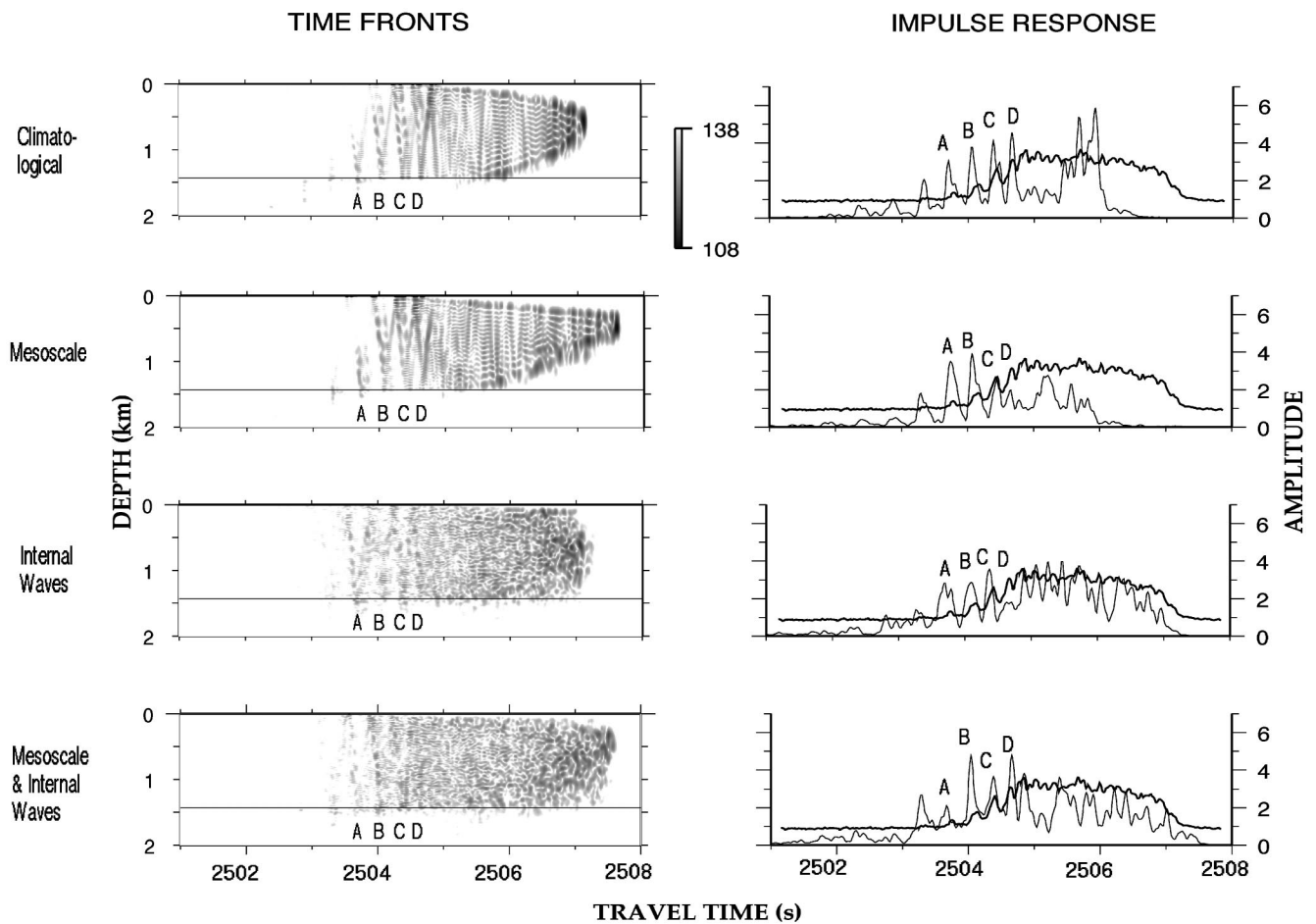

FIG. 4. Composite wavefronts (gray scale with 30-dB dynamic range) and impulse response functions at the receiver range for the different modeling environments used. The computed impulse response functions (thin solid curves—right column) are plotted on an arbitrary scale. The Kaneohe data (solid lines), taken 29 November, 1983, have been incoherently averaged. The importance of scattering due to ocean structure is clearly visible in the lower two panels. The amplitudes of the data were scaled by comparison to the amplitudes of the modeled output arrivals A–D computed by propagation through the climatological sound speed field. Finally, the scaled data were translated along the time axis to give the optimal fit to the arrivals A–D. Note the horizontal line in the left panels is at the hydrophone depth for the impulse response functions shown in the right panels.
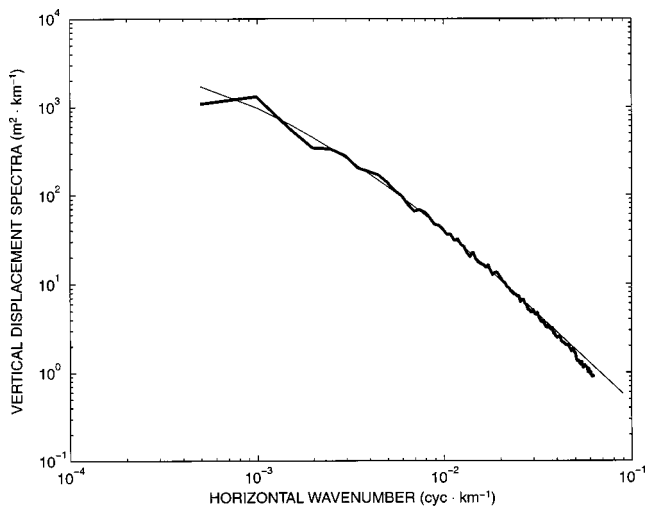
FIG. 5. Power spectral density of vertical displacement of internal waves as a function of horizontal wave number. The thin solid curve is the theoretical estimate given by $\Sigma_{j=1}^{50} F_\zeta(k,j)$ from Eq. (A9), and the thick solid curve is the spectrum calculated from a single realization of a two-dimensional horizontal field 80×80 km in extent, centered at 31.1258 °N, 215.7255 °E, or about 1715 km from the Kaneohe source along the section in Fig. 1.

$$c(x_i, z_j) = \bar{c}(x_i, z_j) + \delta c(x_i, z_j), \qquad (1)$$

where $\bar{c}(x_i, z_j)$ is either the climatological or mesoscale sound speed field.

Various tests assist in validating our internal wave model. Figure 5 illustrates good agreement between simulation and theory [Eq. (A9)] for the power spectral density of vertical displacement as a function of horizontal wave number at a depth of 490 m. The standard deviation of vertical displacement, computed at all depths from a single realization, follows the expected theoretical values [in accordance with Eq. (B7)], except near the surface and bottom (Fig. 6). Because the WKB approximation inherent in the GM spectrum is only applicable in the interior of the turning depths for the internal displacement modes, agreement should not
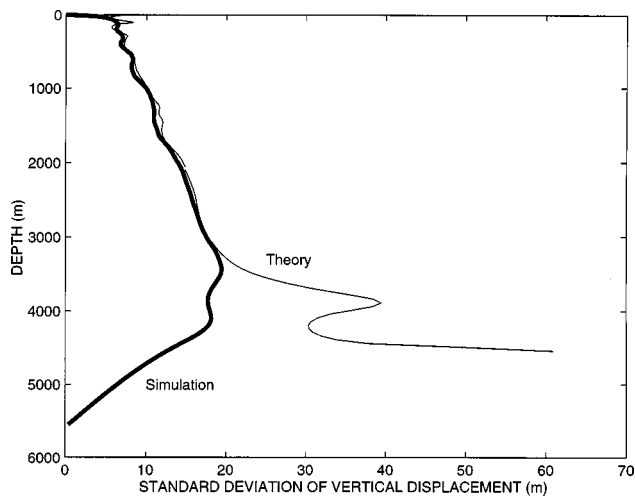

FIG. 6. Standard deviation of the internal wave's vertical displacement as a function of depth. The thin curve is $\langle \zeta^2 \rangle^{1/2} = [\int dk \Sigma_j F_\zeta(k,j)]^{1/2} = [b^2 E_0 N_0 / (2N(z))]^{1/2}$ from Eq. (B7). The thick curve is $\langle \zeta^2 \rangle^{1/2}$, calculated from a single three-dimensional realization of a vertical displacement field, centered at 31.1258 °N, 215.7255 °E.
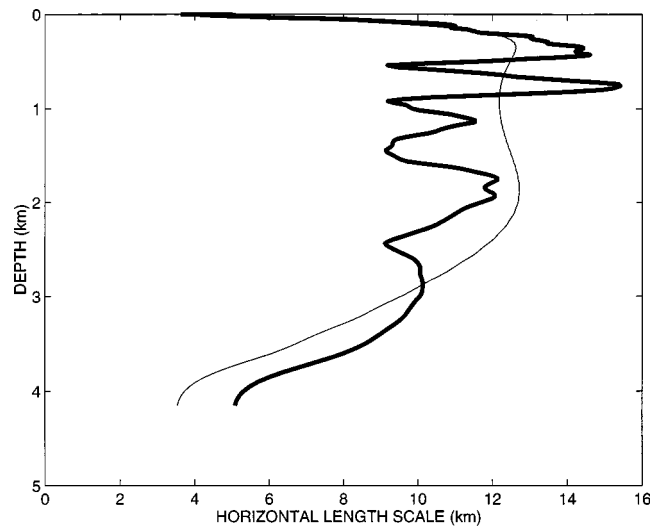

FIG. 7. Horizontal correlation length scale. The thick line is constructed using a single three-dimensional 80×80 km realization of a vertical displacement field, centered at 31.1258 °N and 215.7255 °E, using a discretized form of Eq. (B12) for $\alpha = 0$ and $\pi/2$ radians, then taking the average of the results from these two angles. The theoretical expression, Eq. (B13), is used to produce the thin solid line.

be expected above and below the turning depths. For the realization used, most of the modes have turning depths above 3000 m, and below this depth the zero displacement boundary condition is seen to dominate. The same explanation applies near the surface, except that the upper turning depth is so close to the surface on the depth scale shown that the zero displacement boundary condition and turning depth dependence nearly coincide.

The horizontal correlation length scale is also computed, and a formula for this scale is derived in Appendix B 2. Figure 7 illustrates a reasonable fit between this formula and a single three-dimensional realization of an internal wave field. The high amount of variance shown in the simulation is attributed to the fact that the horizontal extent of the realization is only 80 km, less than eight times the internal wave length scale of $O(10)$ km. Smaller variance is expected for larger section sizes, but 80 km appeared to be the appropriate size; small enough to satisfy the slowly varying assumption for the range dependence of $\bar{c}(x_i, z_j)$ required by our model, and large enough to simulate acoustically relevant horizontal scales of internal gravity waves.[15] The qualitative aspects of a single section of sound speed fluctuations are seen in Fig. 8.

This completes the description of how the ocean sound speed fields (a) through (d) are computed. The next section describes the model which simulates acoustic propagation through these four environments.

III. FULL-WAVE MODELING

For simulating two-dimensional full-wave acoustic propagation over long ranges (>1000 km) in weakly range dependent waveguides, models based on "the parabolic equation method" (PE) are often desirable.[16,17] Note that by "weakly" the problem is assumed to be describable by the physics of multiple forward scattering, as stated in the Intro-
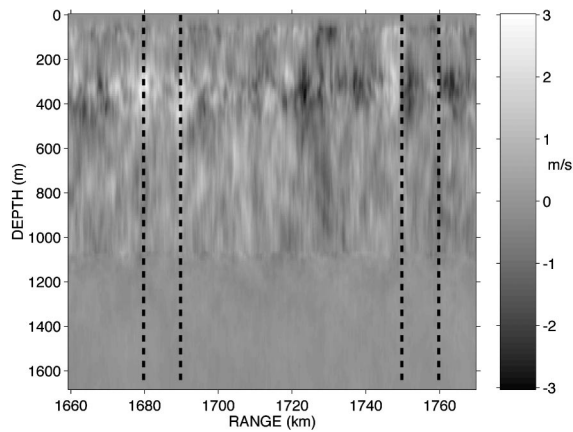
FIG. 8. A realization of a vertical section of sound speed perturbations from internal waves. The value of z_{bot} for this simulation is 4205 m. This field incorporates 50 vertical modes and 128 horizontal wave numbers. The vertical lines indicate the horizontal extent of the section (80 km) and extent of overlap (10 km) as described in Appendix A 2. Only the upper 1640 m are shown.

duction. This desirability is primarily due to the fact that numerical algorithms to solve the wave equation in parabolic form are vastly more efficient than numerical algorithms which solve the Helmholtz wave equation directly (e.g., coupled modes). Further efficiency is obtained by invoking the split-step Fourier algorithm.[18] Most parabolic approximations that implement the split-step algorithm have solutions that depend on a reference sound speed c_0, or are limited to handling acoustic energy confined to small grazing angles ($<15°$). These models have phase errors that accumulate with range, effectively distorting the wavefront and thus yielding errors in the relative and absolute travel times.[19] Our full-wave simulations of the Kaneohe experiment require an algorithm that is insensitive to the reference sound speed and allows for grazing angles up to 90°. The reasoning is the following: The stable early arrivals A–D (see Sec. IV) have travel times that are about 0.4 s later than either what full-wave or ray trace models predict. This discrepancy is probably due to climatic temperature changes in the North Pacific ocean which stem from westward propagating Rossby waves linked to El Niño and the Southern Oscillation.[7] Because these early arrivals are the only stable data, they are used as an anchor for lining up the simulation results and data on a single time scale. The travel time of the late arriving energy, which is attributed to vertical scattering, must then be measured as accurately as possible relative to the early stable arrivals. This dictates that errors in travel times due to sensitivities to grazing angle and/or reference sound speed be minimal. Thus a PE model is used which yields travel times within a few milliseconds accuracy for all the contributing multipaths.[19,20]

A. Pulse synthesis

The method used to synthesize wavefronts and impulse response functions is described in Sec. IV of Tappert *et al.*[20] This method would suffice for comparison with impulse response data for a single pulse transmission, but as mentioned in Sec. I, the data have been incoherently averaged over a day.[1] Besides enhancing the stable arrivals, daily incoherent

averaging also broadens these arrivals due to the ''washing out'' of the wavefront time wandering effect from the passage of internal gravity waves.[5] To simulate this broadening of the data, a running average is performed recursively on the impulse response function. If $I(t_n)$ denotes the square modulus of the complex envelope of acoustic pressure at the discrete time t_n, then the averaging technique employed can be expressed as

$$I(t_n) = \tfrac{1}{4}I(t_{n-1}) + \tfrac{1}{2}I(t_n) + \tfrac{1}{4}I(t_{n+1}). \qquad (2)$$

The sampling interval was chosen to be $t_n - t_{n-1} = 16$ ms. Running this filter recursively for four iterations suffices to broaden the stable arrivals so as to agree with the widths of the measured stable arrivals, which are about 100 ms.[1]

B. Model input parameters

Some of the more relevant environmental parameters required by the PE model include the computational depth H, number of depth points N, and range step dr. The methods for determining both N and dr are described in Appendix C 1. The computational depth chosen is 8000 m, large enough to allow accurate modeling of sub-bottom interactions, but small enough to minimize computational time.

The shallow bathymetry near the source and receiver allows for significant sub-bottom interaction. For this reason, it is particularly important to model the sub-bottom reasonably well. The PE model used allows for a single sediment layer, modeled as a fluid, with linear sound speed gradient and constant density. Relevant input parameters concerned with sub-bottom interaction of acoustic energy include (1) sediment thickness, (2) sediment density, (3) sound speed ratio at the water–sediment interface, (4) gradient of sound speed in the sediment, and the (5) coefficient of volume attenuation in the sediment.

Because the receiver is at 1433 m depth on a continental rise, some of the acoustic energy contributing to the acoustic multipaths penetrates into the sub-bottom. The steeper ($>10°$), early arriving energy penetrates deeper into the sub-bottom than the later energy, which is in general less steep ($<3°$). The question arises as to how to select the sediment parameters for this situation when only a single sediment layer is modeled. Our solution involves forming a composite wavefront from different simulations that use optimal geoacoustic parameters for energy with both steep and shallow grazing angles (refer to Appendix C 2 for details).

The acoustic propagation model and ocean environments having been described, the next section will discuss and interpret the results of the simulations, as they relate to the data.

IV. MODEL RESULTS AND COMPARISON WITH DATA

Two-dimensional full-wave simulations were performed through the four sound speed fields described in Sec. II. The two-dimensional approximation is valid in this case because a three-dimensional calculation would change the travel time by $O(1)$ ms (Sec. IV of Ref. 1). The synthesized wavefronts and impulse response functions at the receiver depth are shown in Fig. 4. The horizontal line in the left panels of Fig.

4 indicate the receiver depth, so that the impulse responses in the right panels are representative of ''cuts'' of the wavefronts at this depth. The daily incoherently averaged impulse response data, taken 29 November 1983, are superposed for qualitative comparison. The results of the simulations are now presented in the order that they are presented in Fig. 4.

A. Climatology

The modeled wavefront in the top panel of Fig. 4 comes from propagation through a climatological sound speed field. This sound speed field is constructed using Levitus data collected over the months of May, June, and July. The weak range dependence in the environment is revealed in the tail of the wavefront, where distinct modes are evident. Taking into consideration the results from ray tracing,[1] the amplitudes of arrivals A–D are seen to be primarily due to acoustic energy that is initiated in large positive vertical wave numbers. This energy initially is surface reflected, then bottom reflected off the Kaneohe slope, and is finally bottom reflected near the receiver (refer to Fig. 9 of Ref. 2). In the geometric ray representation, the initial launch angle corresponds to about 15°.[7] Positive launch angles and grazing angles are defined to be positive upward in the direction toward the receiver.

Inspection of the modeled impulse response reveals small humps on the right of arrivals A and C. These appear to be remnants of the corresponding negative launch angles near −15°, but they are attenuated due to strong bottom interaction near the source. These humps are likely due to acoustic energy that is initially bottom reflected, then surface refracted, and finally bottom reflected near the receiver. To confirm this, a simulation is performed using the same sound speed field, but with the sound speed ratio at the water–sediment interface along the Kaneohe slope set to 1.03, instead of the previous value of 1.02. This gives a critical angle of about 16° instead of the previous value of 11.4°, so that the −15° grazing energy reflects off the bottom, effectively bringing up the hump adjacent to arrival A (not shown).

B. Mesoscale

The wavefront computed from propagation through mesoscale structure indicates strong stability for arrivals A–D (second panel of Fig. 4). Notice also that the envelope of this wavefront has a markedly different shape as compared to that for the pulse propagated through the climatological sound speed field. Especially significant is the time extension of almost 1/2 s in the tail of the wavefront, as compared with the wavefront computed by propagation through the climatology sound speed field (upper panel of Fig. 4).

In geometric acoustics, the travel time change for a single ray that has evolved through unperturbed and perturbed ocean environments can be decomposed into linear and nonlinear components.[22,23] Here, the climatological and mesoscale sound speed fields are considered to be the respective unperturbed and perturbed environments. Denote δT_1 as the total change in travel time, and δT_2 and δT_{NL} as the respective linear and nonlinear components of the change in travel time. Then
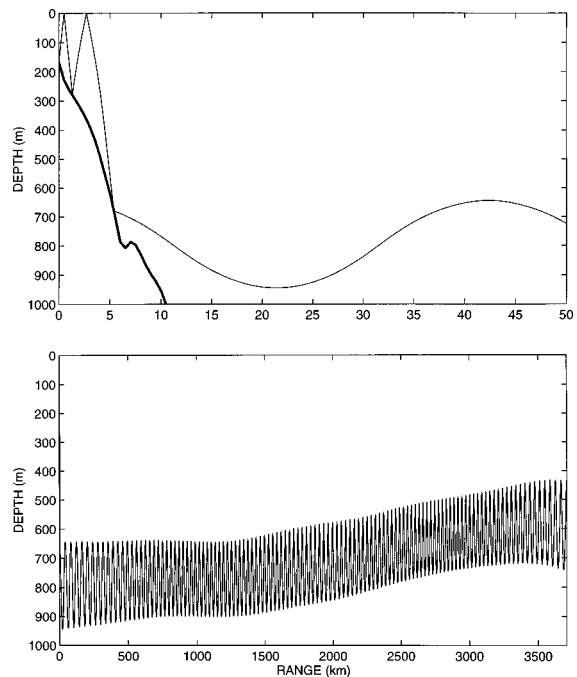

FIG. 9. Path (thin solid line) for the most axial ray through the climatology sound speed field. The upper panel shows the path near the source, and the lower panel shows the entire path. Bathymetry is shown as a thick solid line on the top panel.

$$\delta T_1 = \delta T_2 + \delta T_{NL}. \tag{3}$$

Simulations performed using a ray trace code[1] reveal that the ray with a launch angle of 19.154 degrees has a travel time equal to the cutoff time for the wavefront associated with the climatological environment. This ray's path, shown in Fig. 9, is used to calculate the linear contribution as

$$\delta T_2 \doteq -\int_{\Gamma_0} \frac{\delta c(s)}{c_0^2} ds, \tag{4}$$

where Γ_0 is the path through the climatological sound speed field, $c_0(s)$ and $\delta c(s)$ represents the sound speed perturbation due to the mesoscale structure, and ds is an increment of Γ_0.[22,23] We get

$$\delta T_2 = -0.17 \, \text{s}. \tag{5}$$

The total travel time change is computed directly from the full-wave simulations. The cutoff time for propagation through the climatological environment is $T_0 = 2507.17 \, \text{s}$ (wavefront in first panel of Fig. 4), and the cutoff time for propagation through the mesoscale environment is $T_1 = 2507.61 \, \text{s}$ (wavefront in second panel of Fig. 4), so that

$$\delta T_1 \doteq T_1 - T_0 = +0.44 \, \text{s}. \tag{6}$$

Then

$$\delta T_{NL} = +0.61 \, \text{s}. \tag{7}$$

This leads us to conclude that the total travel time difference seen in the tail of these wavefronts is due primarily to a nonlinear change in travel time. The nonlinear change is an order of magnitude greater than what other simulations report at ranges of about 3000 km for steep energy.[22] This is intriguing, especially since the observed mesoscale structure

TABLE I. Modeled travel times to the nearest 10 ms for peaks A through D through the indicated ocean environments. The travel times from a ray trace model through the mesoscale environment are indicated for comparison (Ref. 1). The climatological average environment is from the spring season of Levitus, and the mesoscale environment is derived from a July 1988 CTD survey.

Ocean environment	Model	Peak travel times (s)			
		A	B	C	D
Climatological	PE	2503.70	2504.06	2504.38	2504.67
Mesoscale	PE	2503.74	2504.07	2504.45	2504.65
	ray	2503.75	2504.09	2504.41	2504.68
Internal waves	PE	2503.74	2504.09	2504.37	2504.66
Mesoscale and internal waves	PE	2503.67	2504.03	2504.38	2504.66

is weak, i.e., $\delta c_{rms} = 0.6$ m/s. The nonlinear term is only computed for a single realization of mesoscale structure. If one investigates the month-to-month data and measures the time between the multipath arrival A and the latest arriving acoustic energy, it is seen that the cutoff times are not sensitive to changes in the mesoscale structure. For example, Fig. 3 of Ref. 2 illustrates the cutoff times for data recorded over consecutive days in 1983 and one day in 1987. This supports the interpretation that the nonlinear component of the total travel time change is a bias. However, it must be recognized that the impulse response data were recorded at a depth well below the axis of the sound channel. It is not certain how the month-to-month cutoff time variability at a depth of 1433 m correlates with the cutoff time variability at the axis depth (which is about 600 m at the receiver range). This adds some uncertainty to our interpretation.

This interpretation of travel time bias has been investigated for steeper ray paths at ranges up to 3000 km,[22] where it was first shown that the magnitude of the bias is insensitive to the location of the eddies. The bias was shown to have either a plus or minus sign, and had magnitudes of up to about 50 ms, much less than what we observe for the latest arrivals.

C. Internal waves

The two lower panels of Fig. 4 illustrate the wavefronts associated with pulse propagation through internal waves superposed with the climatology and mesoscale environments. Notice that the ''accordionlike'' behavior of the early portion of the wavefronts that is so readily apparent in the upper panels is still observed in the lower panels. The lower caustics of this accordion contribute to the arrivals A–D, as seen in the adjacent impulse response curves. So, it can be concluded that internal waves of nominal strength do not destroy the inherent stability in arrivals A–D (see Table I). Of course, that is to be expected, since this stability is noticed in the data.

The next detail to observe is the strong vertical scattering in the tail portion of the wavefronts in the lower two panels. Internal waves of nominal strength are seen to be a likely candidate for contributing to the vertical scattering the axial energy over one kilometer in extent. The final cutoff in the impulse response curves (right lower panels of Fig. 4) is seen to better match the data, as compared to the wavefronts resulting from propagation through an environment without internal waves.

The lower two panels of Fig. 4 indicate that the positive nonlinear change in travel time due to the observed mesoscale structure swamps any travel time bias induced from internal waves. According to Dashen et al.,[24] the internal wave induced bias should be proportional to the logarithm of the acoustic frequency times the square of the propagation range times the strength of the internal waves. Results reported from Colosi et al. (refer to Table IV of Ref. 5) at 1000-km range, using twice the nominal GM internal wave strength and an acoustic center frequency of 250 Hz, indicate an internal wave induced bias in the tail of the wavefront of −4 ms. Extrapolating these results to our simulations, one expects an internal wave induced bias of about −24 ms. This is indeed much smaller than the total travel time change of 440 ms due to the mesoscale structure. Notice also that the cutoff time is extended by an additional 1/4 s in the impulse response that is derived from propagation through an environment composed of mesoscale structure superposed with internal waves (lowest panel of Fig. 4), as compared with propagation through an environment composed of a climatological sound speed field superposed with internal waves (third panel of Fig. 4).

All the impulse response curves in Fig. 4 show that absolute travel times of arrivals A–D are similar, within about 40 ms in all simulations (Table I). Simulations performed using different realizations of internal wave fields yielded similar results (not shown). Arrivals A–D changed their travel time by less than 10 ms, although their amplitudes varied by as much as 50%. This corroborates the observation that steep energy is less affected by sound speed fluctuations than energy with shallow grazing angles.[5]

V. VERTICAL SCATTERING

When the horizontal stratification of the ocean waveguide is broken by weak volume inhomogeneities, due to, for example, internal waves, an acoustic pulse undergoes multiple forward scattering. A consequence of this is the spreading in depth of acoustic energy, which we refer to as vertical scattering. Recently, an ''outer intensity envelope'' of the wavefront has been used to illustrate the extent of vertical scattering due to propagation through volume inhomogeneities, such as internal waves.[5] This intensity envelope is constructed from a wavefront of acoustic transmission loss by interpolating the minimum and maximum depth where the transmission loss assumes a predefined cutoff value. This is
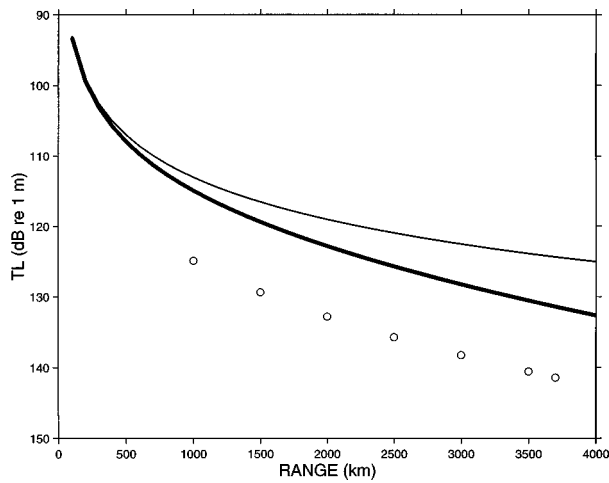
FIG. 10. Transmission loss as a function of range for geometric spreading (thin solid), geometric spreading plus absorption (thick solid), and the intensity cutoff values (circles) used for computing the outer intensity envelopes of Fig. 11.

done throughout the time domain of the wavefront, which depends on the dynamic range of intensity chosen *a priori*. Comparing the envelopes constructed from simulations with and without internal waves gives a measure of the extent of vertical scattering. Here, we take this idea one step further, inquiring how the extent of vertical scattering changes as a function of range.

The measure of vertical scattering as a function of range depends on the dynamic range and reference level of intensity chosen. It is also dependent on which portion of the pulse is chosen. This paper is primarily interested in the vertical scattering of the late arriving ''axial'' acoustic energy. Other parameters affecting the measure of vertical scattering may include the source bandwidth and center frequency, pulse length, and integration time. To clarify the relevant issues, the following thought-experiment is posed: The same Kaneohe experiment is performed, but instead of the single hydrophone, vertical arrays of hydrophones are arranged along the geodesic every 500 km in range. Signal enhancement is performed via incoherent averaging, just as described by Spiesberger and Tappert.[1] If the ocean structure could be turned off and on, what would be the amount of vertical scattering measured due to ocean structure at the range of each vertical array?

If the acoustic energy is contained within the waveguide (i.e., bottom interactions are assumed negligible), then, in an adiabatic environment, the total transmission loss at any field point is due solely to spreading loss and volume absorption. Sound interacts with the bottom near the source and receiver, but away from these regions, bottom interactions are negligible. In a nonadiabatic environment, the principal additional mechanism that affects transmission loss is multiple forward scattering.

As usual for adiabatic waveguide environments, the spreading is assumed spherical out to a range of about 5 km, then cylindrical beyond.[25] Taking into account the linear growth of the number of arrivals at any particular depth (we assume a growth rate of 0.02 arrivals per km,[25] or an average ray loop distance of 50 km), the transmission loss due to

spreading is slightly less than, but proportional to, spherical. The transmission loss due to absorption for sub-kilohertz frequencies is predominantly due to boric acid relaxation, and is linear with range (the absorption coefficient is about 1.2 dB/1000 km, see Refs. 2, 26). The cutoff value chosen to construct the envelopes for the wavefronts is 10 dB greater than the transmission loss due to spreading and absorption (Fig. 10).

The tails of the outer envelopes are shown in Fig. 11 at 500-km intervals, starting at 1000 km. The environments used for these simulations are the climatological sound speed field and a structured ocean consisting of internal waves superposed with the mesoscale sound speed field. Two observations are worth mentioning: (1) The envelopes shoal toward the surface with range, following the trend of the sound channel (Fig. 4 of Ref. 1); (2) The extent of vertical scattering is seen to markedly increase beyond the range of 2000 km.

VI. DISCUSSION

Full-wave simulations using a parabolic equation model demonstrate that internal waves, eddies, and bottom characteristics can account for the strong vertical scattering ob-
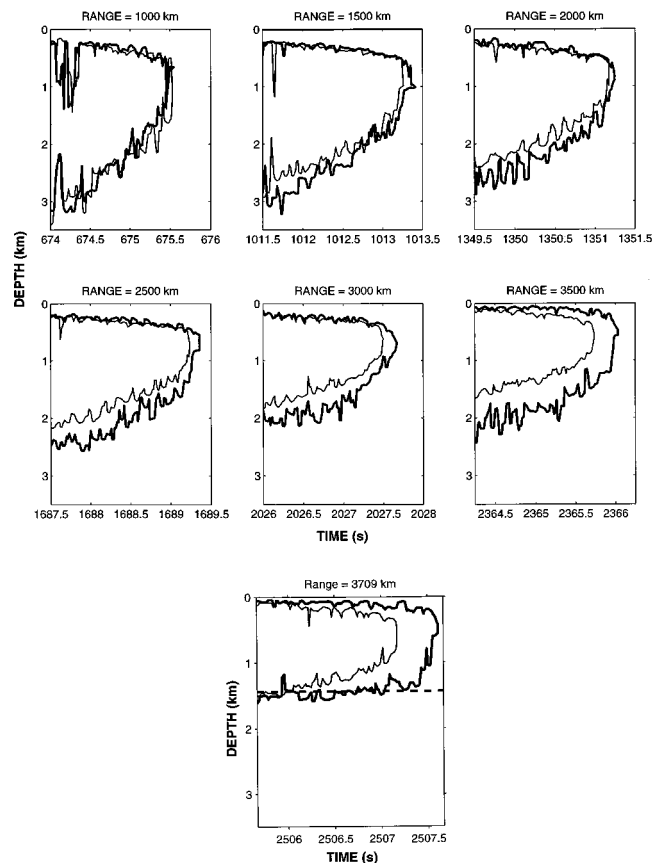

FIG. 11. Outer intensity envelopes of wavefronts at various ranges along the section indicated in Fig. 1. The thin solid curves represent the outer intensity envelopes derived from propagation through the climatological environment, and the thick solid curves represent the outer intensity envelopes derived from propagation through an environment composed of mesoscale with a realization of internal waves superposed. Only the final 1.5–1.75 s of the tail are shown at the indicated ranges, each in a 2-s window. The thick dashed line in the last panel indicates the bottom depth at the receiver range.

served for acoustic pulse-like signals of 133-Hz, 60-ms resolution at the range of 3709.21 km. The internal wave model is range dependent and fully three dimensional, based on the internal wave spectrum of Garrett and Munk.[12,13] The effects of internal waves, mesoscale structure, and bottom interactions are adequate to explain the Kaneohe data.

In our simulations, we strived to avoid ''tuning'' the model to fit the data. The sub-bottom and bathymetry near the source and receiver need to be modeled reasonably well to account for the relative differences in amplitudes seen in the data, but as one would expect, arrival times were not sensitive to how the sub-bottom is modeled. However, the simulations performed did not include the effects of rough bottom scattering near the source. It is not known to what extent the final cutoff time seen in the impulse response data is sensitive to bathymetric features with range scales below one kilometer. Thus our results regarding scattering are consistent with the data, but the scattering of sound from a rough bottom has not been explored in a quantitative manner. It seems that the actual effects of the rough bottom would be suppressed because sound does not actually travel along thin rays. Instead, sound propagates within eigentubes[21] whose broader scales would insonify larger swaths of the bottom.

Oceanic mesoscale structure significantly extend the cutoff in the tail of the wavefront, and it was demonstrated that this wavefront tail extension is attributed to a nonlinear change in travel time. The observations are consistent with a bias interpretation for this nonlinear component of travel time change, and this effect will have to be taken into account if these data are used in tomographic inversions. The stable arrivals A–D, however, are insignificantly affected in regards to travel time (see Table I and Fig. 4). This is in agreement with the relatively small bias $[O(50)$ ms] reported for steep, early arrivals at ranges of 3000 km.[22] This supports previous evidence that arrivals A–D are useful for measuring temperature.[1,2,7]

APPENDIX A: MODEL FOR SIMULATING INTERNAL WAVE FIELDS

This Appendix provides a detailed prescription as to how the sound speed fluctuations due to internal waves are numerically generated.

1. Simulating a single section

Let ζ denote the vertical displacement of a water parcel due to small amplitude internal waves, with positive ζ indicating downward displacement. Recall that the depth z is defined as positive downward, with $z=0$ at the surface. Then the contribution to the total sound speed field due to internal waves is

$$\delta c(x,z,t) = -\left(\frac{\partial \overline{c}(z)}{\partial z}\right)_{\text{pot}} \zeta(x,z,t), \qquad (A1)$$

where $(\partial \overline{c}(z)/\partial z)_{\text{pot}}$ is the climatologically averaged potential sound speed gradient computed at the middle of a section. The potential sound speed gradient is defined as

$$\left(\frac{\partial \overline{c}}{\partial z}\right)_{\text{pot}} = \left(\frac{\partial \overline{c}}{\partial z}\right) - \left(\frac{\partial \overline{c}}{\partial z}\right)_{a}, \qquad (A2)$$

where the second term on the right-hand side is the adiabatic sound speed gradient. In the ocean, the adiabatic sound speed gradient is expressed in terms of temperature, T, pressure, P, and salinity, S, as

$$\left(\frac{\partial \overline{c}}{\partial z}\right)_{a} = \left(\frac{\partial \overline{c}}{\partial P}\right)\left(\frac{\partial P}{\partial z}\right)_{a} + \left(\frac{\partial \overline{c}}{\partial T}\right)\left(\frac{\partial T}{\partial z}\right)_{a}, \qquad (A3)$$

where the second term on the right-hand side is negligible. Both $\partial \overline{c}/\partial z$ and $\partial \overline{c}/\partial P$ are calculated using Levitus' database and Del Grosso's sound speed formula.[8,9] Linear interpolation is used to provide the potential sound speed gradient at any depth of interest.

The field of vertical displacements due to internal waves is described statistically as a sum over internal wave vertical displacements modes $W(j,k,z)$,[15] where j is the mode number index and k is the magnitude of the horizontal wave number vector. The vertical modes and corresponding eigenfrequencies, $\omega(j,k)$, satisfy the Sturm–Liouville problem[27,28]

$$\frac{d^2 W}{dz^2} + \left(\frac{N^2(z) - \omega^2}{\omega^2 - \omega_i^2}\right) k^2 W = 0, \qquad (A4)$$

with boundary conditions

$$W(z=0) = W(z=z_{\text{bot}}) = 0, \qquad (A5)$$

where z_{bot} is the range averaged ocean bottom depth, $N(z)$ the buoyancy frequency, and ω_i the inertial frequency, all determined at the center of a section. The eigenfunctions are orthonormal over their natural weighting $N^2(z) - \omega_i^2$. The buoyancy profile is determined from

$$N^2(z) = -g\rho^{-1}\partial_z\rho - \frac{g^2}{\overline{c}(z)^2}, \qquad (A6)$$

where g is gravity, and ρ is the density of sea-water, which is computed according to Fofonoff.[29]

Let y be the horizontal spatial coordinate perpendicular to x, and let k_1 and k_2 be the respective x and y components of the horizontal wave number vector; i.e., $k = \sqrt{k_1^2 + k_2^2}$. Then, without any further approximations, a three-dimensional, time dependent field of vertical displacements due to small amplitude internal wave motions is described by

$$\hat{\zeta}(x,y,z,t) = \mathcal{D}^{-1} \text{Re} \left\{ \int_{-\infty}^{\infty} dk_1 \int_{-\infty}^{\infty} dk_2 Q(k_1, k_2, z, t) \right.$$

$$\left. \times \exp(ik_1 x) \exp(ik_2 y) \right\}, \qquad (A7)$$

where

$$Q(k_1, k_2, z, t) = (2\pi k)^{-1} \sum_j \sqrt{F_\zeta(k,j)} [A(j, k_1, k_2)$$

$$+ iB(j, k_1, k_2)] W(j, k, z) \exp[i\omega(j,k)t]. \qquad (A8)$$

Choosing $A(j, k_1, k_2)$ and $B(j, k_1, k_2)$ as independent Gaussian random numbers with zero mean and unit variance, the field of vertical displacements will then be a Gaussian random process with zero mean and variance given by the power spectrum $F_\zeta(k,j)$. This spectrum is taken to be consistent with the empirical spectrum of Garrett and Munk,[12,13] given by

$$F_\zeta(k,j) = \zeta_{\text{ref}}^2 \frac{8}{\pi^2} \frac{k^2 k_j}{(k^2 + k_j^2)^2} \frac{j_*}{j^2 + j_*^2}, \qquad (A9)$$

where $k_j = j\pi\omega_i/(N_0 b)$, $N_0 = 3$ cph, $\zeta_{\text{ref}} = 7.3$ m, $j_* = 3$. The parameter b is the buoyancy scale depth in km. The normalization constant $\mathcal{D}$ in Eq. (A7) is set according to

$$\mathcal{D}^2 = (2\pi k)^{-1} \sum_j \int dk F_\zeta(k,j) W^2(j, k, z_{\text{ref}}), \qquad (A10)$$

where z_{ref} is the depth where $N(z_{\text{ref}}) = N_0$. Thus the field will be insured to statistically have the correct variance at every depth. The derivation of Eq. (A9) is provided in Appendix B 1. The two-dimensional field along the geodesic is then simply

$$\zeta(x, z, t) = \hat{\zeta}(x, y = 0, z, t). \qquad (A11)$$

The sound speed fluctuations for a section are computed according to Eq. (A1).

2. Section patching

Let the subscript m denote the mth section of sound speed fluctuations, as in $\delta c_m(x, z, t)$. Also, denote the horizontal extent of each section by X and the extent of overlap for adjacent sections be X_p. The sound speed fluctuation values inside the patching region are computed according to

$$\delta c(x, z, t) = S_m(x) \delta c_m(x, z, t) + S_{m+1}(x) \delta c_{m+1}(x, z, t), \qquad (A12)$$

where

$$S_m(x) = \begin{cases} \cos^2\left[\left(\frac{x - m(X - X_p)}{X_p} \right) \frac{\pi}{2} \right]; \\ \quad \text{if } m(X - X_p) \leq x \leq m(X - X_p) + X_p, \\ 0; \quad \text{otherwise,} \end{cases} \qquad (A13)$$

$$S_{m+1}(x) = \begin{cases} \sin^2\left[\left(\frac{x - m(X - X_p)}{X_p} \right) \frac{\pi}{2} \right]; \\ \quad \text{if } m(X - X_p) \leq x \leq m(X - X_p) + X_p. \\ 0; \quad \text{otherwise.} \end{cases} \qquad (A14)$$

The results reported here use $X = 80$ km and $X_p = 10$ km. After the sections of sound speed fluctuations are patched together, the total sound speed field is computed from Eq. (1).

APPENDIX B: DERIVATIONS OF USEFUL FORMULAS

This Appendix provides derivations of formulas used for simulating internal wave sound speed fluctuations and verifying that the simulations follow the chosen theoretical model.

1. Derivation of power spectrum of vertical displacement

The vertical displacement spectrum, Eq. (A9), follows directly from the Garrett and Munk form expounded on page 285, Eq. 9.19 of Ref. 30. It is expressed in terms of frequency and vertical mode number as

$$f_\zeta(\omega, j) = b^2 \frac{N_0}{N} \left(\frac{\omega^2 - \omega_i^2}{\omega^2} \right) E(\omega, j), \qquad (B1)$$

where the energy density $E(\omega, j)$ is

$$E(\omega, j) = E_0 B(\omega) H(j), \qquad (B2)$$

$$B(\omega) = \frac{2}{\pi} \frac{\omega_i}{\omega(\omega^2 - \omega_i^2)^{1/2}}, \qquad (B3)$$

$$H(j) = \frac{(j^2 + j_*^2)^{-1}}{\Sigma_j (j^2 + j_*^2)^{-1}}. \qquad (B4)$$

The dimensionless internal wave energy parameter E_0 is set to 6.3×10^{-5}, and b is the buoyancy scale depth. The vertical displacement spectrum as a function of magnitude of horizontal wave number vector and vertical mode number is

$$F_\zeta(k,j) = f_\zeta(\omega = \omega(k), j) \frac{d\omega}{dk}, \qquad (B5)$$

where the Jacobian of transformation, $d\omega/dk$, is obtained from the WKB relation $\omega = [(N_0 b/j\pi)^2 k^2 + \omega_i^2]^{1/2}$:[30]

$$\frac{d\omega}{dk} = \left(\frac{N_0 b}{j\pi} \right)^2 \frac{k}{\left[\left(\frac{N_0 b}{j\pi} \right)^2 k^2 + \omega_i^2 \right]^{1/2}}. \qquad (B6)$$

Substituting this expression into Eq. (B5), defining $k_j = j\pi\omega_i/N_0 b$, yields

$$F_\zeta(k,j) = \frac{4}{\pi} \frac{b^2 N_0 E_0}{2N(z)} H(j) \frac{k^2 k_j}{(k^2 + k_j^2)^2}. \qquad (B7)$$

Defining $\zeta_{\text{ref}}^2 = b^2 E_0/2$ to be the reference vertical displacement at the depth $z = z_{\text{ref}}$ where $N(z_{\text{ref}}) = N_0$ eliminates the vertical displacement spectrum's dependence on depth, giving

1303   J. Acoust. Soc. Am., Vol. 106, No. 3, Pt. 1, September 1999

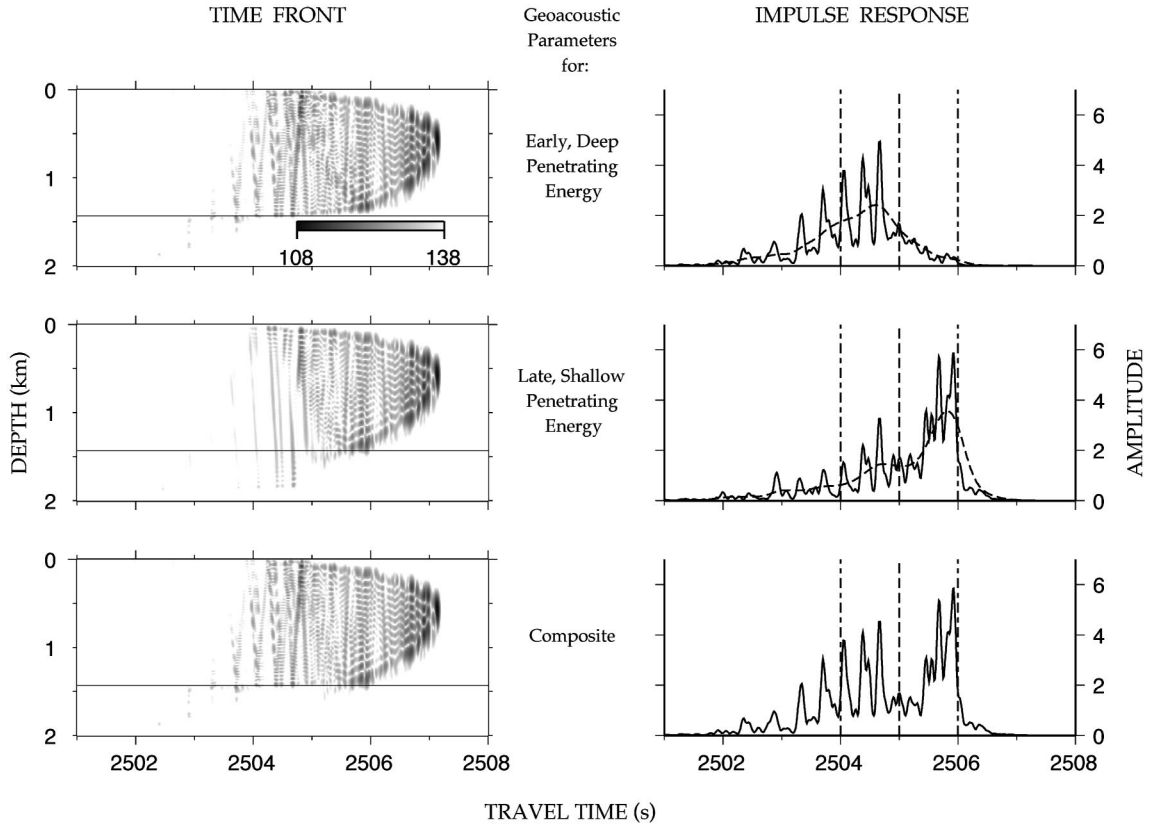M. A. Wolfson and J. L. Spiesberger: Full wave simulation   1303

FIG. C1. Wavefronts and associated impulse response functions at the receiver range for the Levitus environment using bottom parameters that were chosen to model: (1) the early arriving, steep penetrating energy (upper panel); (2) the late, shallow penetrating energy (middle panel). The lower panel shows the composite wavefront and impulse response function constructed by smoothly joining the amplitude of the wavefront after it was Pascal filtered in range over all depths on the PE depth mesh. The smoothing was done using one quarter cycle of a cosine squared window applied over the 2-s record bounded by the vertical long, dash-dotted lines. The short, dash-dotted lines indicate the time where the two different wavefronts were joined. The wavefronts are shown using a gray scale with 30-dB dynamic range and the impulse response functions are shown with an arbitrary amplitude scale. Note the horizontal line in the left panels is at the hydrophone depth for the impulse response functions shown in the right panels.

$$F_\zeta(k,j) = \frac{4}{\pi} \zeta_{\text{ref}}^2 H(j) \frac{k^2 k_j}{(k^2 + k_j^2)^2}. \tag{B8}$$

Equation (A9) is obtained by applying the Poisson summation formula to the normalization of $H(j)$.

2. Derivation of horizontal length scale

Starting from Eq. (A7), without loss of generality, set $t = 0$, and instead of taking the real part of a complex random process, choose the random variables such that $Q(-k_1, -k_2, z, 0) = Q^*(k_1, k_2, z, 0)$. Then, since for each depth the process ζ is spatially homogeneous, aside from the normalization constant, $\mathcal{D}$, the autocorrelation function is related to the power spectral density of $Q(k_1, k_2, z, 0)$ by a Fourier transform,

$$\langle|Q(k_1,k_2,z,0)|^2\rangle = \left(\frac{1}{2\pi}\right)^2 \int_{-\infty}^{\infty} dx' \int_{-\infty}^{\infty} dy' C(x',y',z)$$

$$\times \exp[-i(k_1 x' + k_2 y')], \tag{B9}$$

where $C(x',y',z) = \langle \hat{\zeta}(x,y,z,0)\hat{\zeta}(x+x',y+y',z,0)\rangle$ is the autocorrelation function (the angled brackets denote the ensemble average operator). The inverse relation to this gives

$$C(x',y',z) = \int_{-\infty}^{\infty} dk_1 \int_{-\infty}^{\infty} dk_2 \langle|Q(k_1,k_2,z,0)|^2\rangle$$

$$\times \exp[i(k_1 x' + k_2 y')]. \tag{B10}$$

Equation (B9) is the two-dimensional form of the Wiener–Kinchine theorem.[31] Since the random variables, $A(j,k_1,k_2)$ and $B(j,k_1,k_2)$, are uncorrelated for different vertical modes, j,

$$\langle|Q(k_1,k_2,z,0)|^2\rangle = \sum_j W^2(j,k,z) F_\zeta(k,j). \tag{B11}$$

The horizontal integral scale length is defined as

$$L_H(z) \doteq \frac{\int_0^\infty dr\, C(r\cos\alpha, r\sin\alpha, z)}{C(0,0,z)}, \tag{B12}$$

where $(x',y') = (r\cos\alpha, r\sin\alpha)$, α representing the angle r makes with the x-axis.[32] Substituting Eq. (B11) into Eq. (B10), converting the denominator of Eq. (B12) to polar coordinates, and using the fact that $\langle|Q(k_1,k_2,z,0)|^2\rangle$ is an even function of k_1 and k_2, we obtain

$$L_H(z) = \frac{\int_0^\infty dk\, k^{-1} \Sigma_j W^2(j,k,z) F_\zeta(j,k)}{\int_0^\infty dk\, \Sigma_j W^2(j,k,z) F_\zeta(j,k)}. \tag{B13}$$

TABLE CI. Range step and number of depth points used in PE simulations for the three regions delineated in Fig. 2.

Region	1	2	3
Range (km)	0–200	200–3600	3600–3709.21
N	2048	1024	2048
dr (m)	25	100	25

TABLE CII. Geoacoustic parameters used for generating composite time fronts. The parameter σ denotes the ratio of sound speed at the bottom of the water to that at the top of the sediment.

	σ	ρ_s (kg/m^3)	α (dB/km/kHz)
A–D	1.020	1.8	0.02
Tail	1.002	1.5	0.02

APPENDIX C: SYNTHESIS OF ACOUSTIC WAVE FIELDS

1. Convergence

This Appendix describes the method used to insure convergence of the PE simulation. Additionally, it explains our hybrid method used to synthesize wavefronts when realistic modeling of acoustic propagation in the sub-bottom is required within the constraint of using a PE model. Both of these methods were developed with the primary goal of retaining numerical efficiency as much as possible.

The ocean environment is separated into three regions: (1) a downslope region covering the first 200 km in range; (2) a deep, waveguide region extending from 200 km to 3600 km in range; (3) an upslope region extending from 3600 km to 3709.21 km, the receiver range. Our criterion for convergence is to compare travel times and amplitudes at selected depths at the end of each region for two runs that differ only in either the number of depth points N or range step dr. The selected depths were chosen to be 200, 400, 800, 1000, and 1600 m. The run with the coarser mesh is said to have converged if the travel times and amplitudes, taken over a 40-dB dynamic range (measured down from the maximum intensity) differ by less than 3 ms and 1 dB, respectively.

A low pass filter is applied in the wave number domain of the PE field for each frequency when a smaller number of depth points N is desired; e.g., in going from region 1 to region 2. Similarly, zero padding in the wave number domain is used when a larger number of depth points is desired. The values of dr and N used in each region are summarized in Table CI.

2. Selection of geoacoustic parameters

Because the acoustic propagation model assumes a constant density in a single sediment layer at any given range, and in reality the density is depth dependent, the issue of how to choose the appropriate sediment density arises. There are many ways to resolve this problem. The most obvious way is to allow for a density profile in the sediment, while still incorporating the range dependent c_0-insensitive transformation. Since a model of this form does not exist, our solution was to form a composite of two separate runs, each run using a density appropriate for the two extreme cases; (1) deep penetrating, earlier arriving energy, and (2) shallow, late arriving energy. The wavefronts from each simulation are smoothly joined to form a composite wavefront and associated impulse response curve at the receiver range. Figure C1 summarizes the composition method used synthesizes the presented wavefronts and impulse functions. The relevant geoacoustic parameters used in each case are now described. As in Fig. 8, the horizontal line in the left panels at the

receiver depth reveal that the impulse responses in the right panels are ''cuts'' of the wavefront at this depth.

Using the NGDC database,[33] it was determined that the sub-bottom near the receiver is composed predominantly of a 600-m layer of ooze and silt. Near the water–sediment interface, the density expected to be near 1.5 g/cm^3, with a sound speed gradient close to 1 s^{-1}.[34,35] The ratio of sediment sound speed to water sound speed at the water–sediment interface is about 1.002, yielding a critical grazing angle of 3.6° (Diana McCammon, personal communication). The attenuation coefficient of 0.02 dB/m/kHz is appropriate for this type of sediment and acoustic frequency.[36]

The late arriving, small grazing angle energy in the tail of the pulse only significantly interacts with a small region in depth into the sediment; it is refracted up and out before deep penetration. Here, the values determined above near the water–sediment interface are used. For the steeper arriving energy, deeper bottom penetration is expected and an integrated value of density of 1.8 g/cm^3 is used. To be consistent, a correspondingly larger sound speed ratio of 1.02 is used, yielding a critical angle of 11.4°. Table CII summarizes the geoacoustic parameters in the simulations.

[1] J. L. Spiesberger and F. D. Tappert, ''Kaneohe acoustic thermometer further validated with rays over 3700 km and the demise of the idea of axially trapped energy,'' J. Acoust. Soc. Am. **99**, 173–184 (1996).
[2] J. L. Spiesberger, K. Metzger, and J. A. Furgerson, ''Listening for climatic temperature change in the northeast pacific: 1983–1989,'' J. Acoust. Soc. Am. **92**, 384–396 (1992).
[3] J. A. Colosi and S. M. Flatté, ''Mode coupling by internal waves for multimegameter acoustic propagation in the ocean,'' J. Acoust. Soc. Am. **100**, 3607–3620 (1996).
[4] J. A. Colosi, ''Random media effects in basin-scale acoustic transmissions,'' in *Monte Carlo Simulations in Oceanography*, pp. 157–166. A'ha Huliko'a Hawaiian Winter Workshop, University of Hawaii at Manoa, 1997.
[5] J. A. Colosi, S. M. Flatté, and C. Bracher, ''Internal-wave effects on 1000-km oceanic acoustic pulse propagation: Simulation and comparison with experiment,'' J. Acoust. Soc. Am. **96**, 452–468 (1994).
[6] T. Vincenty, ''Direct and inverse solutions of geodesics on the ellipsoid with application of nested equations,'' Surv. Rev. **176**, 88–94 (1975).
[7] J. L. Spiesberger, H. E. Hurlburt, M. Johnson, M. Keller, S. Meyers, and J. J. O'Brien, ''Acoustic thermometry data compared with two ocean models: The importance of Rossby waves and ENSO in modifying the ocean interior,'' Dyn. Atmos. Oceans **26**, 209–240 (1998).
[8] S. Levitus, ''Climatological atlas of the world ocean,'' in NOAA Prof. Pap. 13. U.S. Government Printing Office, Washington, DC, 1982.
[9] V. A. Del Grosso, ''New equation for the speed of sound in natural waters with comparisons to other equations,'' J. Acoust. Soc. Am. **56**, 1084–1091 (1974).
[10] J. B. Bowlin, J. L. Spiesberger, T. F. Duda, and L. F. Freitag, ''Ocean acoustical ray-tracing software ray,'' Technical report, Woods Hole Oceanographic Institution, 1992.
[11] National Geophysical Data Center, Boulder, CO, ''5 minute gridded world elevations and bathymetry—a digital database,'' 1987.
[12] C. Garrett and W. Munk, ''Space-time scales of internal waves,'' Geophys. Fluid Dyn. **2**, 225–264 (1972).

1305   J. Acoust. Soc. Am., Vol. 106, No. 3, Pt. 1, September 1999

M. A. Wolfson and J. L. Spiesberger: Full wave simulation   1305

[13] C. Garrett and W. Munk, ''Space-time scales of internal waves: a progress report,'' J. Geophys. Res. **80**, 291–297 (1975).

[14] L. B. Dozier and F. D. Tappert, ''Statistics of normal mode amplitudes in a random ocean,'' J. Acoust. Soc. Am. **63**, 353–365 (1978).

[15] S. Flatté, R. Dashen, W. Munk, K. Watson, and F. Zachariasen, *Sound Transmission Through a Fluctuating Ocean* (Cambridge University Press, Cambridge, 1979).

[16] M. Leontovich and V. Fock, ''Solution of the problem of propagation of electromagnetic waves along the earth's surface by the parabolic equation method,'' Zh. Eksp. Teor. Fiz. **16**, 557–573 (1946).

[17] Frederick D. Tappert, *The Parabolic Approximation Method*, edited by J. B. Keller and J. S. Papadakis (Springer-Verlag, New York, 1977), pp. 224–287.

[18] F. D. Tappert, K. B. Smith, and M. A. Wolfson, ''Analysis of the split-step Fourier algorithm for the solution of parabolic wave equations,'' Math. Modeling Sci. Comp. (in press).

[19] F. D. Tappert and M. G. Brown, ''Asymptotic phase errors in parabolic approximations to the one-way Helmholtz equation,'' J. Acoust. Soc. Am. **99**, 1405–1413 (1996).

[20] F. D. Tappert, J. L. Spiesberger, and Linda Boden, ''New full-wave approximation for ocean acoustic travel time predictions,'' J. Acoust. Soc. Am. **97**, 2771–2782 (1995).

[21] J. Bowlin, ''Generating eigenray tubes from two solutions of the wave equation,'' J. Acoust. Soc. Am. **89**, 2663–2669 (1997).

[22] J. L. Spiesberger, ''Ocean acoustic tomography: Travel time biases,'' J. Acoust. Soc. Am. **77**, 83–100 (1985).

[23] W. Munk and C. Wunsch, ''Biases and caustic in long-range acoustic tomography,'' Deep-Sea Res. **32**, 1317–1346 (1985).

[24] R. Dashen, S. M. Flatté, and S. A. Reynolds, ''Path-integral treatment of acoustic mutual coherence functions for ray in a sound channel,'' J. Acoust. Soc. Am. **77**, 1716–1722 (1985).

[25] W. Munk, P. Worcester, and C. Wunsch, *Ocean Acoustic Tomography* (Cambridge University Press, Cambridge, 1995).

[26] C. S. Clay and H. Medwin, *Acoustical Oceanography: Principles and Applications* (Wiley, New York, 1977).

[27] C. Eckart, *Hydrodynamics of the Oceans and Atmospheres* (Pergamon, New York, 1960).

[28] O. M. Phillips, *The Dynamics of the Upper Ocean* (Cambridge University Press, Cambridge, 1977).

[29] N. P. Fofonoff, ''Physical properties of sea-water,'' in *The Sea*, Volume 1, edited by M. N. Hill (Interscience Publishers, New York, 1962), Chap. 1.

[30] C. Wunsch and B. Warren, *The Evolution of Physical Oceanography* (MIT Press, Cambridge, 1981).

[31] R. L. Stratanovich, *Topics in the Theory of Random Noise*, Vol. 1 (Gordon and Breach, New York, 1963).

[32] V. I. Tatarski, *Wave Propagation in a Turbulent Medium* (Dover, New York, 1961).

[33] D. L. Divins and B. Eakins, ''Total sediment thickness map for the Southeast Pacific Ocean,'' in Intergovernmental Oceanographic Commission, edited by G. B. Udintsev, International Geological-Geophysical Atlas of the Pacific Ocean (in press).

[34] E. L. Hamilton, ''Sound velocity-density relations in sea-floor sediments and rocks,'' J. Acoust. Soc. Am. **63**, 366–377 (1978).

[35] E. L. Hamilton, ''Sound velocity gradients in marine sediments,'' J. Acoust. Soc. Am. **65**, 909–922 (1979).

[36] E. L. Hamilton, ''Sound attenuation as a function of depth in the sea floor,'' J. Acoust. Soc. Am. **59**, 528–536 (1976).